Journal of Microscopy, Vol. 228, Pt 2 2007, pp. 153–164
Received 4 December 2006; accepted 4 May 2007

Simultaneous false-colour imaging of birefringence, extinction and transmittance at camera speed

W. KAMINSKY, E. GUNN, R. SOURS & B. KAHR
Department of Chemistry, University of Washington, Seattle, WA 98195, USA

Key words. Amyloid plaque, birefringence, cholesteryl acetate, crystal quality assessment, dichroism, electro-optic effect, extinction, human hair, optical polarimetry, polarized light, water flea.

Summary

A polarized light imaging technique is introduced that simultaneously captures and unfolds transmittance, fast/slow axes directions and birefringence or linear dichroism from single camera exposures. The technique, based on the rotating polarizer method, is capable of sampling an object through polarizers at four different angles in a single image with the use of an image multiplexer. The range of possible applications is demonstrated with examples from the fields of biology, medicine, forensics and material sciences.

Introduction

For more than two centuries, polarized light microscopes have been used to study linear birefringence and linear dichroism in all manner of organized media. Methods for imaging linear optical anisotropies are used by engineers to model strain (Ajovalasit *et al.*, 1998), by manufacturers for quality control in textile production (Litwin & Sadik, 1998; Hamza *et al.*, 2002; Zeitner *et al.*, 2003), by forensic scientists (Velez, 2003) and by physicians engaged in microstructural analyses of tissues (e.g. de Boer *et al.*, 1997, 1999; Saxer *et al.*, 2000), among others. However, deriving quantitative information from the colourful images delivered by the polarizing microscope has required the use of additional components such as optical retarders while aligning the sample with the polarimetric reference system of the microscope (Hartshorne & Stuart, 1964).

Methods have been developed for the measurement of two-dimensional images of linear birefringence and directions of the fast and slow axes (extinction, φ) based on optical modulation (Noguchi *et al.*, 1992; Mei & Oldenbourg, 1994; Oldenbourg & Mei, 1994, 1995; Otani *et al.*, 1994; Bajor, 1995; Glazer *et al.*, 1996; Shribak, 1996; Glazer & Cosier, 1997; Shribak *et al.*, 1999; Yeh *et al.*, 1999; Zhu *et al.*, 1999; Geday *et al.*, 2000; Zhu *et al.*, 2002; Owen & Garman, 2005). Tilting a uniaxial crystal sample has also produced three-dimensional maps of birefringence and eigenrays (Pajdzik & Glazer, 2006). As shown by Shribak & Oldenbourg (2003), separation of birefringence, extinction and transmittance can be achieved by employing incident circular polarization and a sequence of four measurements with linear polarizer settings at 0°, 45°, 90° and 135°. However, one of the drawbacks of currently available birefringence imaging systems is the lag time required for the sequential acquisition, analysis and display of each image, limiting their use in high-volume settings (i.e. in polymer quality assessment, in silicon carbide wafer production, or in re-crystallizations frequently used in pharmacological and other synthesis processes) that would benefit from real-time analysis.

Here, the four measurements typically collected sequentially are captured simultaneously as the quadrants of a single image. Asundi *et al.* (2001) attempted this before to image birefringence in real time by employing a set of quarterwave retarders at different orientations placed in each of the four light paths of the image multiplexer. However, our approach differs from the previously published work in employing four polarizers instead of retarders. In so doing, we are able to overcome the problems outlined by Asundi and co-workers related to image resolution, registration and accuracy, where the sampling rate is principally limited only by the time resolution of the imaging system itself (~20 ms if an ordinary CCD camera of 640 × 480 pixel resolution is used). Furthermore, offline analysis on images obtained with super-fast photographic techniques allows time resolutions of 1 μs or less.

We describe the use of a specially designed software package that, in conjunction with the commercial image multiplexer,

Correspondence to: Dr. W. Kaminsky. Tel: 206 543 7585; fax: 206 685 8665; e-mail: kaminsky@chem.washington.edu

permits the real-time analysis and simultaneous display of microscopic images, encoding in false colours three different aspects of a sample: (1) the absolute value of the sine of the phase factor $\delta = 2\pi\Delta nL/\lambda$, where Δn is the linear birefringence, L is the sample thickness and λ is the wavelength of the light; (2) the eigenray directions via the extinction angle φ and (3) the transmittance.

The prototype described here, 'Milliview', has a temporal resolution of 35 ms in the off-line mode (28 triplet micrographs per second). In the on-line (real-time) mode, the software produces triplets with a repetition rate of 10 per second on a 2.6-GHz PC. This is a major improvement over existing technology. A commercial device such as Metripol, from Oxford Cryosystems, has a temporal resolution of 10 s or more per triplet. PolScope from CRI requires sampling times of several seconds.

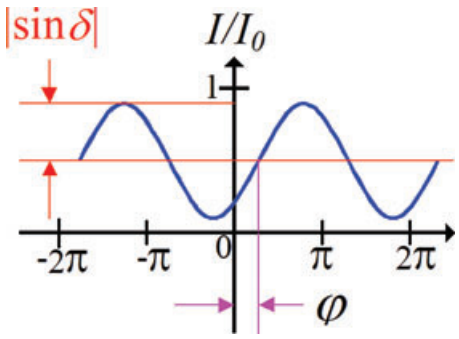

Fig. 2. Variation of intensity and optical parameters in the rotating polarizer method. The phase angle ωt for a continuously varying rotating polarizer is replaced by discrete polarizer settings α_i in the Milliview technique.

Methods

The basic design of Milliview is illustrated in Fig. 1. It implements a commercial microscope for polarized light (ML9300, Meiji Techno America, Santa Clara, CA, USA) to which an interference filter and broadband quarter-wave retarder (Edmund Optics USA, Barrington, NY, USA) were added.

The Quadview image multiplexer from MAG Biosysems (MAG Biosystems, Tucson, AZ, USA) was attached to the C-mount of the microscope. The arrangement of polarizers (there are 16 different possible configurations) is optimized to compensate as much as possible for the polarizing effects of the mirror system of the Quadview. The image is recorded via a 480 × 640 pixel CCD camera (COHU, Inc, San Diego, CA, USA, Cat 4915-2010) and connected to a PC via a video card (Viewcast/Osprey, Planto, TX, USA) with a driver that supports the Video for Windows (VFW) format. There are no other moving parts on the device than those present on a basic polarized light microscope. The images are computed with custom software that runs on a PC with the Microsoft Windows XP operation system.

The concept of operation (Eqs (1) and (2)) has been published previously (Glazer *et al.*, 1996). The intensity of a retarding sample between a circular polarizer and a linear polarizer (Fig. 2) at N angles α_i is

$$I_i = \frac{I_0}{2}[1 + \sin 2(\alpha_i - \varphi)\sin\delta]. \qquad (1)$$

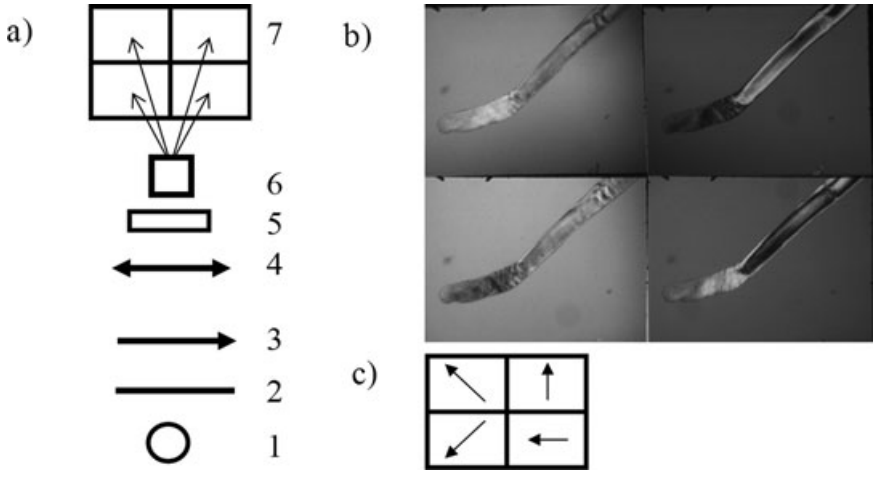

Fig. 1. (a) Schematic of Milliview optical path. 1: light source, 2: interference filter, 3: polarizer, 4: quarter wave-plate, slow axis at 45° towards the preferred direction of the polarizer, 5: sample. 6: Quadview image multiplexer, 7: CCD camera with in-four split copies of the image of the sample and four polarizers at angles of 0°, 45°, 90° and 135° with respect to the coordinate system of the microscope. Optical lenses are not shown as they are part of a standard polarizing microscope (including 1 and 3). (b) Four simultaneous images of a human white hair seen through polarizers at four angles as shown in (c) indicated by black arrows.

Recasting this equation into a linear polynomial results in

$$
\begin{aligned}
&I_i = a_0 + a_1 \sin 2\alpha_i + a_2 \cos 2\alpha_i,\\
&\alpha_i = \alpha_{\max}/N; \alpha_{\max} = 180^{\circ},\\
&a_0 = \tfrac{1}{2} I_0,\\
&a_1 = \tfrac{1}{2} I_0 \sin\delta \cos 2\varphi,\\
&a_2 = -\tfrac{1}{2} I_0 \sin\delta \sin 2\varphi,\\
&a_0 = \sum_{i=1}^{N} \tfrac{1}{N} I_i; a_1 = \sum_{i=1}^{N} \tfrac{2}{N} I_i \sin 2\alpha_i; a_2 = \sum_{i=1}^{N} \tfrac{2}{N} I_i \cos 2\alpha_i.
\end{aligned} \tag{2}
$$

When intensities are measured for angles $2\alpha_i$ covering full periods of the sinusoidal functions, the system of equations is already diagonal and can be solved without the involvement of an explicit matrix inversion. A four-image multiplexer with polarizers placed at 0°, 45°, 90° and 135° with respect to a horizontal reference gives measured intensities I_1, I_2, I_3 and I_4, respectively, per pixel of the CCD camera. Thus, we find

$$
\begin{aligned}
&a_0 = \sum_{i=1}^{4} \tfrac{1}{4} I_i; \quad a_1 = \sum_{i=1}^{4} \tfrac{2}{4} I_i \sin 2\alpha_i = \tfrac{1}{2}(I_2 - I_4);\\
&a_2 = \sum_{i=1}^{4} \tfrac{2}{4} I_i \cos 2\alpha_i = \tfrac{1}{2}(I_1 - I_3).
\end{aligned} \tag{3}
$$

The birefringence (Δn) is embedded in $|\sin(\delta)|$, which is calculated as follows:

$$
|\sin\delta| = \frac{1}{a_0}\sqrt{a_1^2 + a_2^2}. \tag{4}
$$

The extinction angle φ (varying from 0 to π measured counter-clockwise from the horizontal) is given by

$$
\varphi = \frac{\pi}{2} + \operatorname{sgn}(a_2)\tfrac{1}{2}\arccos\left(\frac{-a_1}{\sqrt{a_1^2 + a_2^2}}\right). \tag{5}
$$

The sample transmittance, varying from 0 (opaque) to 1 (no absorption), is simply

$$
(a_0). \tag{6}
$$

A feature of (5) is that the accuracy of φ depends only on the value of $|\sin(\delta)|$; φ is not defined if δ is close to a multiple of π, in which case the orientation is encoded in black.

The images thus computed are then represented in false colours. It is clearly visible in Fig. 1 that the four quadrants are illuminated differently and slightly rotated towards each other but maintain equal size. Prior to applying the algorithm outlined earlier, the quadrant images have to be aligned and additional corrections have to be applied before representing the final images as in Fig. 3.

Image registration is critical to this application to achieve a perfect match of the four images. The mapping of the images should be simple to prevent a slowing of the algorithm. Thus, employing any of the open-source software packages for this purpose is not recommended. After the total image has been captured and transformed into a data array, the top-left quadrant is scanned pixel by pixel (position x_1, y_1). To find the corresponding pixels of, for example, the top right quadrant, the indices (position x_2, y_2) of that quadrant are obtained according to the following transformation:

$$
x_2 = x_1 + c_x + 320 - \frac{y_1}{k}; \quad y_2 = y_1 + c_y + x_1\frac{240}{320}\frac{1}{k}, \tag{7}
$$

where the three sets of adjustable values (k, c_x, c_y) correct the misorientation between the quadrants (see Fig. 4c for the meaning of k, c_x and c_y).

The software (Fig. 5) written for this application consists of a routine where each of the quadrants is shown together with the

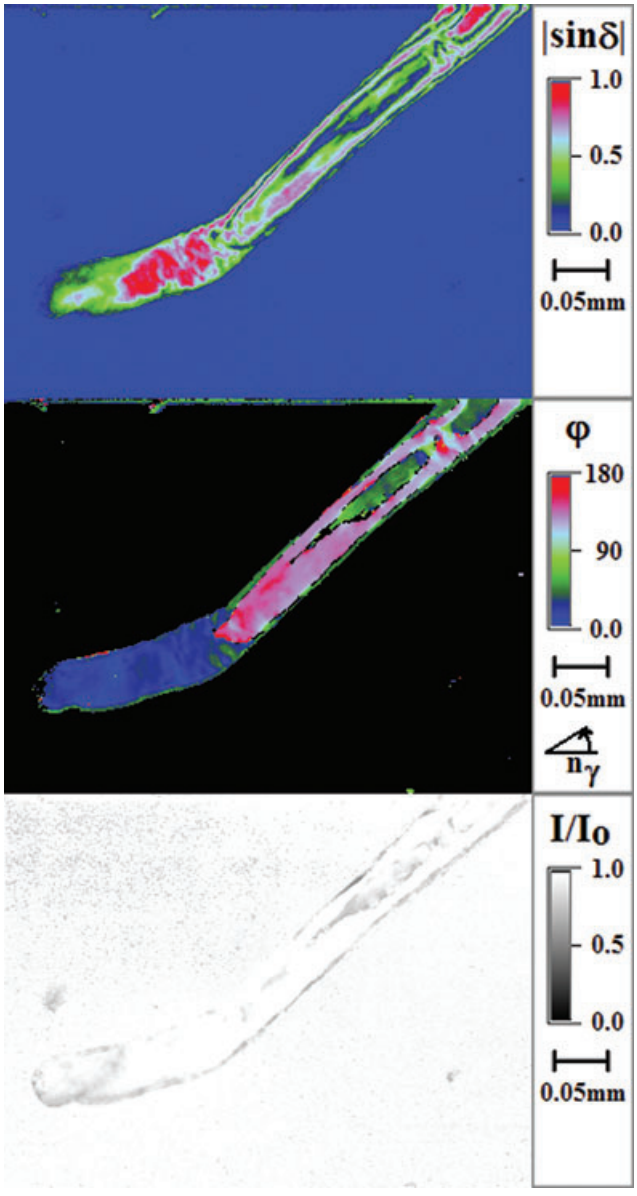

Fig. 3. Deconvolved image of $|\sin(\delta)|$, extinction φ, and transmittance I/I_o of the hair shown in Fig. 1b collected at a wavelength of 550 nm.

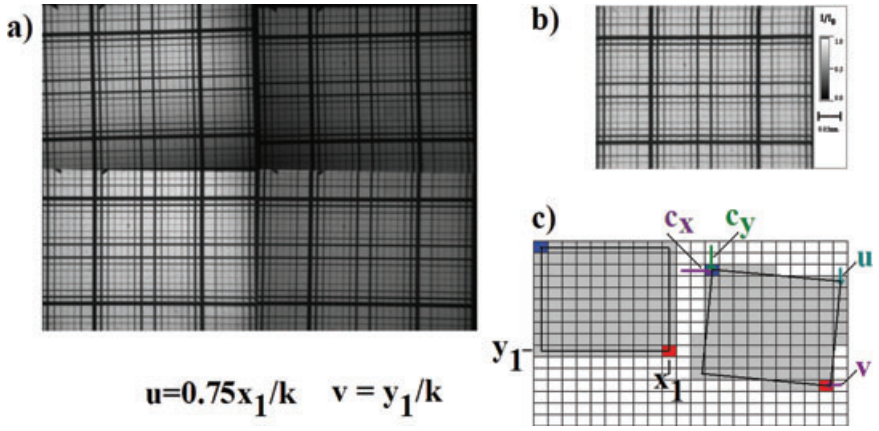

Fig. 4. (a) A non-polarizing object used to align the four quadrants. (b) All four quadrants overlaid using Eq. (7). (c) Graphical interpretation of the mapping parameters c_x, c_y and k for an image aspect ratio of 0.75 (= 240/320). A pixel (highlighted in red) at point (x_1, y_1) is mapped to the corresponding pixel (in red) of the distorted quadrant by calculating new indices from a horizontal shift by the image width plus fixed positional shifts c_x, c_y and variable rotation shifts u and v.

reference image (top-left quadrant) and the parameter triplet k, c_x and c_y of the selected quadrant is adjusted manually until the representation of a test-object overlaps completely (Fig. 4). This procedure has to be done only once as part of the general calibration process of the system as long as the mechanical adjustment of the mirrors in the image multiplexer itself does not change. The correction is valid over the range of microscope foci.

In addition to inhomogeneous illumination, the use of the Quadview image multiplexer introduces unwanted parasitic retardations, causing the resulting image of $|\sin(\delta)|$ to become dependent on φ. By taking a calibration curve $s(\varphi)$ for a quarter-wave retarder as sample, the measured $|\sin(\delta)|$ is scaled for each pixel according to $|\sin(\delta)|' = |\sin(\delta)|/s(\varphi)$. Naturally, the size of each of the micrographs is only a quarter of the size of the CCD image.

In addition, the whole image is normalized by a sample-free background intensity image and each quadrant ($i = 1, \ldots, 4$) of the image, is scaled by factors s_i to yield the same minimum and maximum intensity readings which insures a residual $|\sin(\delta)|$ of close to 0.001(1) for near-perfect incident circular polarized light everywhere across the image (550 nm, no sample). Because the signal is insensitive to the sign of δ, a value of $|\sin(\delta)| = 0.001(1)$ represents a residual noise level for the linear differential retardation of approximately 0.08 nm at that wavelength.

The linearity of the method is satisfactory, as shown in Fig. 6 with maximum deviations from perfection of $\Delta|\sin(\delta)| = \pm 0.05$. The maximum order in $|\sin(\delta)|$ where the readings start to deviate significantly is related to the bandwidth of the interference filter. In the case shown in Fig. 6, a filter of 50 nm bandwidth limits the maximum phase factor δ to approximately 20. For filters of 20 nm bandwidth or less, much higher values are correctly measured.

Since all four quadrant images are collected at the same time, intensity fluctuations caused by the illumination system or camera gain drifts are cancelled out (see Eqs 4 and 5). Given sufficient light intensities, only the noise level of the camera impacts the signal-to-noise ratio. Thus, the Milliview method can produce images of high quality at a fraction of the exposure times otherwise required for sequential devices that are also strongly subject to the aforementioned fluctuations.

The software produces large amounts of data that can be stored as bitmaps and AVI files (audio–video interleaved), or compressed and stored in a zip-file to save disk space. All steps of the algorithm are outlined in the flow chart in Fig. 5.

Examples

Overview

Examples of the application of Milliview follow, including

1. The study of a living cyclops water flea from freshwater ponds of the American Northwest.
2. Rapid screening of Alzheimer's disease amyloid plaques from human brain tissue.
3. Determination of cholesterylacetate crystalline spherulite growth rates.
4. Imaging of the linear electro-optic effect in ammonium dihydrogen phosphate ($(NH_4)H_2PO_4$ (ADP)) exposed to an alternating electric field.
5. Measurement of linear dichroism in a phthalic acid crystal dyed with methyl red.

Cyclopoid copepods

Milliview was tested first on a living organism as a proof of concept. Some cyclops water fleas (cyclopoid copepods)

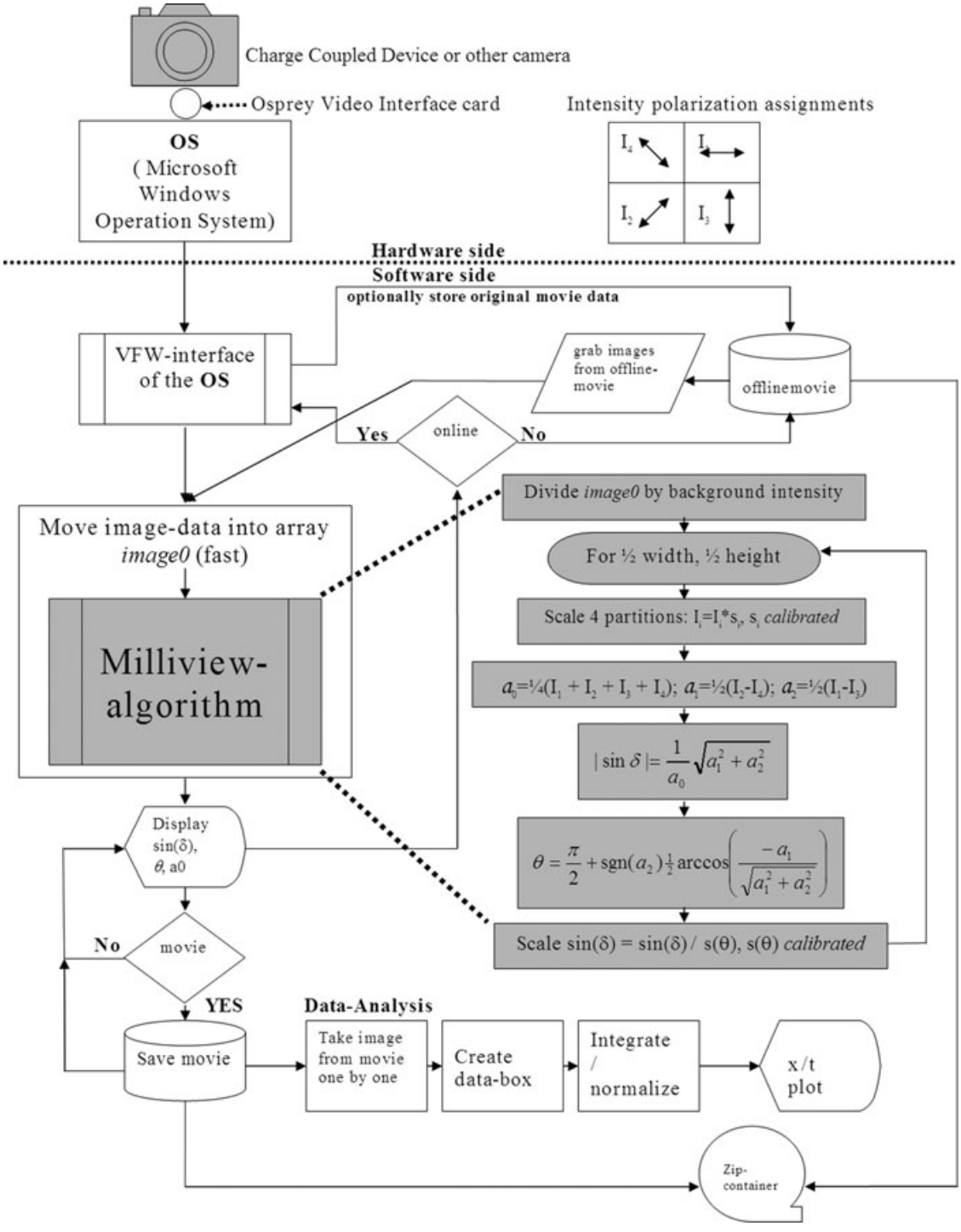

Fig. 5. Flowchart describing the Milliview software.

were collected from a nearby pond and trapped between a glass slide with a shallow depression and a thin cover slip, leaving enough fresh water to keep the flea alive for hours and leaving space for it to roam about before being returned to an aquarium. Members of the family *cyclopidae* (Brandl, 2005) are characterized by the antennulae, the number of segments as well as its singular eye (Fig. 7).

Milliview was used to study internal muscular motion cycles (Fig. 8). The extinction image highlights different morphological details compared with the transmittance

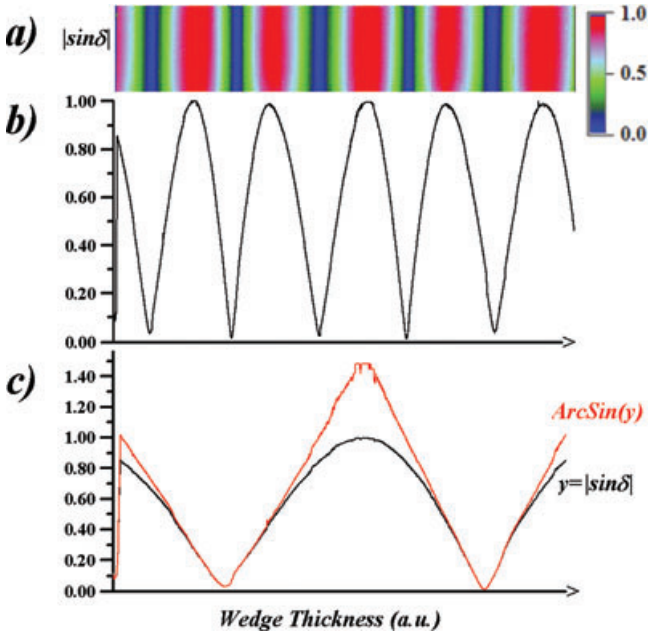

Fig. 6. Fringe pattern of a quartz wedge (composite image from 30 individual measurements). (a) Colour-coded |sin (δ)| as a function of wedge thickness covering approximately three orders; a minimum wedge thickness causes |sin (δ)| to start at a non-zero value. (b) |sin (δ)| as measured per pixel, integrated over the image height. (c) The linearity of $\delta = \arcsin(|\sin(\delta)|)$ for roughly the first order. The wedge was aligned horizontally to allow better placement in the graphic. However, the result does not change if the wedge is rotated to a different φ-angle and scanned along that direction. The slow axis direction φ obtained from the algorithm needs a further adjustment via a calibration curve to limit systematic deviations to approximately 0.5°.

and birefringence images. Where the pigmented eye is the dominant feature in transmittance map, the disparate segments of the chitin shell are highlighted in groups of uniform intensity. Muscle fibre is strongly birefringent and contributes to contrast in the |sin (δ)| images.

Clinical screening

For screening of samples by eye, at least 10 images per second are required to follow the movement of an object on a computer screen. When the sampling rate is just 3 times or less per second, one tends to become increasingly impatient and sampling rates of 1 or more seconds is intolerable for longer studies.

Milliview was put to the test in the search for amyloid plaques in a pathologic brain tissue sample of a deceased Alzheimer's disease patient (Jin *et al.*, 2003). The microscope was operated in on-line mode with 100 ms sampling time. Figures 9a and b show an accumulation of plaques that are characterized by their birefringence and extinction patterns, recognizable at a small magnification (10×). The plaques have disordered cores with small values of |sin (δ)| and radial patterns in

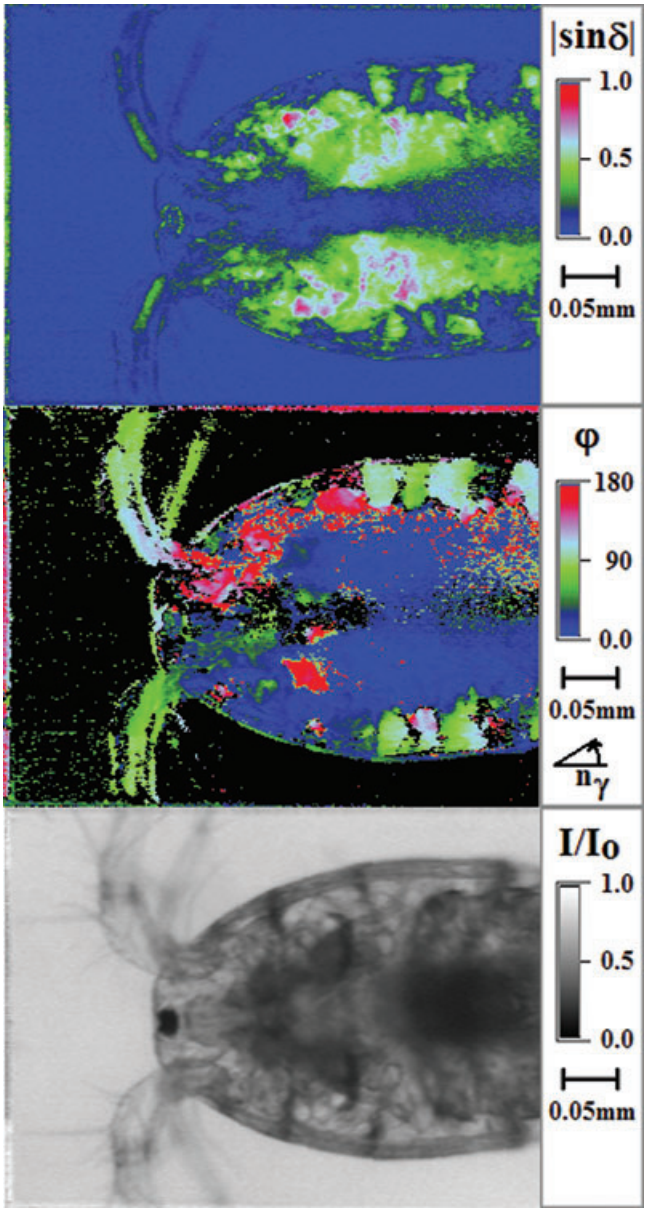

Fig. 7. Cyclops water flea. Bottom: The single eye, which gave the species its name, is completely dark in the transmittance I/I_o. Top: |sin (δ)| showing mainly muscle. Middle: Extinction φ related to organ groups. Images were collected at a wavelength of 550 nm.

the extinction as seen in the progressive variation in the corresponding false colours. The magnified plaque in Fig. 9c shows more detail, demonstrating a good signal-to-noise ratio, especially when considering that the images were obtained within 100 ms.

Kinetics of cholesteryl acetate crystal growth

Crystals have been the quintessential samples for the development of polarized light imaging (Kaminsky *et al.*,

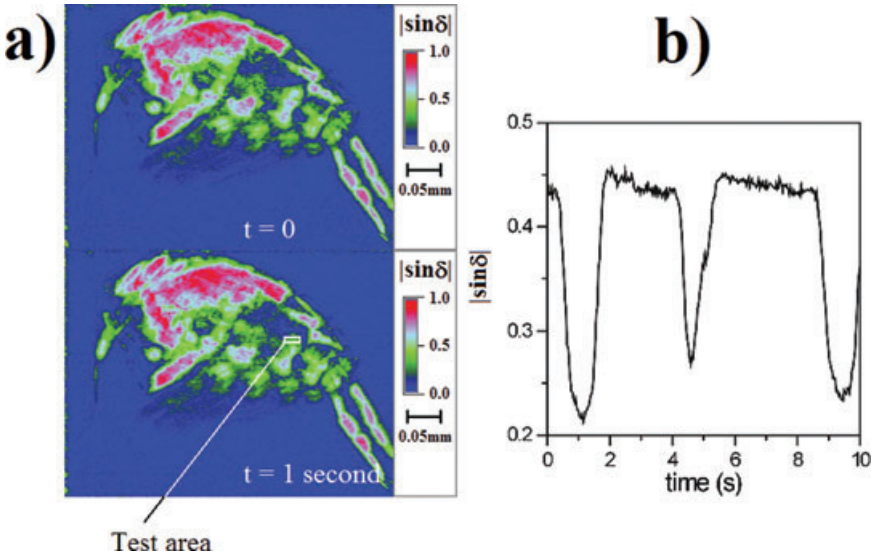

Fig. 8. Cyclops water flea on its side. (a) False -colour images of $|\sin(\delta)|$. The top and bottom images were separated by 1 s with a sampling time of 20 ms. (b) The line chart shows the change of birefringence over time in the test area caused by muscle contraction. The sample area was placed where the largest differences in $|\sin(\delta)|$ occurred. A total of 280 images were collected (in offline mode) covering 10 s. Images were collected at a wavelength of 550 nm.

2004). The images in Fig. 10 show the growth of cholesteryl acetate over 5 s. Cholesteryl acetate, like Alzheimer's disease amyloid plaques, is spherulitic in form when grown from the melt. A mixture of 80:20 cholesterylacetate–cholesterylbenzoate was heated to 180°C, at which point the liquid crystals that formed were pressed between a slide and cover glass. The material was cooled at a rate of 0.5°C s^{-1}. Spherulites appeared at roughly 65°C.

Electro-optic effect

The linear electro-optic or Pockels effect is characterized as a change of refraction when an electric field is applied. Crystals tend to show a change in birefringence that reflects the symmetry of the structure.

$(NH_4)H_2PO_4$ (ADP) shows relatively large electro-optic responses (Fig. 11). Milliview was set in conoscopic imaging mode by the insertion of a standard Amici-Bertrand lens to focus the image onto the back-focal plane. An electric field was applied along the optic axis [001] of a 1-mm-thick (001) sample plate via transparent electrodes (ITO) using Canada Balsam/isopropyl alcohol as electrolytic optical cement.

The result is a 'split' of the optic axis of the uniaxial crystal in directions [110] and $[\bar{1}10]$ that causes ADP to become optically biaxial. The maximum change of birefingence normalized to the electric field can be used to calculate the electro-optic coefficients.

The retardation is defined as $G = L\,(n'' - n')$. In ADP, the change in retardation ΔG is related to the applied voltage U_3 along [001], so that $G(U) = G + \Delta G$. The electro-optic coefficient r_{123} and refractive index $n_{11} = n_o$ with polarization perpendicular to [001] is, according to Haussuehl (1983)

$$\Delta G = -n_{11}^3 r_{123} U_3. \tag{8}$$

The signal measured with Milliview results from a change of $|\sin(\delta)|$ with phase factor $\delta(U_3) = 2\pi(G+\Delta G)/\lambda$ as follows:

$$\Delta|\sin\delta| = |\sin\delta(U_3^+)| - |\sin\delta(U_3^-)|. \tag{9}$$

The maximum effect is observed for δ around an area with the lowest phase factor for applied voltage U^- in the vicinity of the optic axis. Calculation with r_{123} (ADP) = 8.6 pm V^{-1} (Landolt-Boerrnstein, 1969), $n_{11} = n_o = 1.525$ (600 nm, Zernicke, 1964) and an applied voltage of $U_3 = 1000$ V at $\lambda = 550$ nm gives $\delta(U_3) = 0.348$. The maximum change of $|\sin(\delta)|$ observed in the centre of the conoscopic image is 0.29(1). When normalized to the maximum amplitude at that direction for conoscopic imaging of $|\sin(\delta)|$ of 0.9(1), this translates to a $\delta(U_3)$ of 0.33(2).

As shown, several factors have to be addressed before using this approach to measure electro-optic responses quantitatively. Although undoubtedly already of value to find the absolute orientation of the sample (differentiating between *a* axis and *b* axis in ADP for selected sample orientation towards the electric field), an accurate measurement of the electro-optic effect must account for the decreased amplitude of the $|\sin(\delta)|$ signal and the effect of increased optical paths and additional polarization effects at larger conoscopic angles as outlined by Geday & Glazer (2004)[1]. However, the conoscopic

[1] Such a decrease is *not* observed for higher values of δ when in orthoscopic configuration.

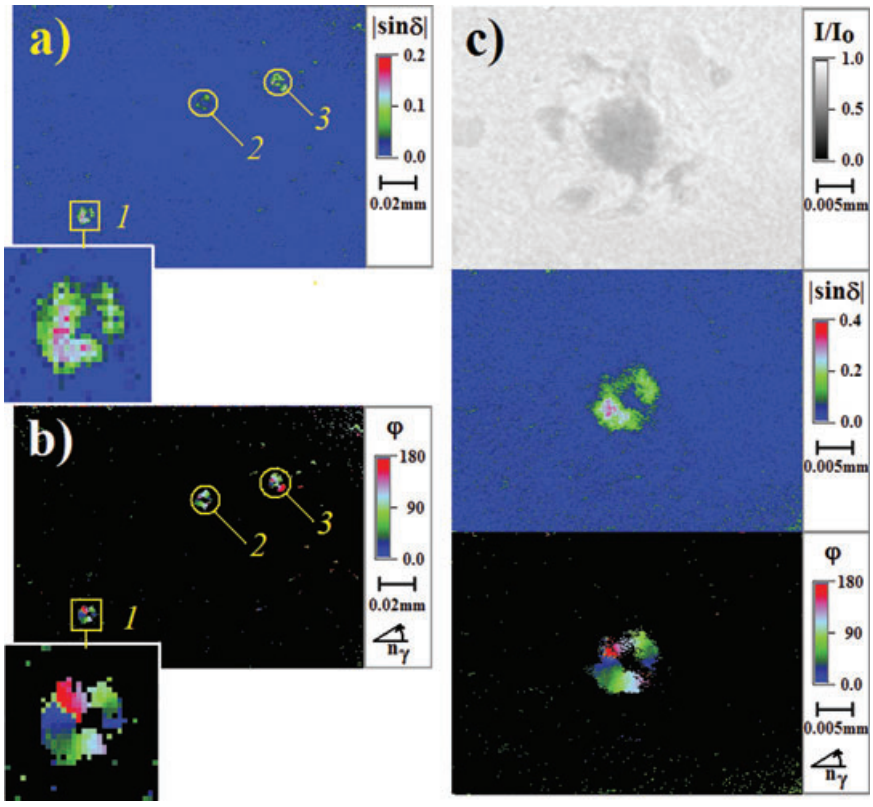

Fig. 9. Amyloid plaques (1, 2, 3) embedded in 8-μm brain tissue section, stained with the histochemical dye Congo red. (a), (b): The sampling rate in on-line mode is 10 frames per second. The identification of amyloidosis is based on the observed birefringence pattern with a typical 'hole' of reduced birefringence in the centre of the plaque and the radial distribution of the slow axis. The images of $|\sin(\delta)|$ and extinction (φ) show three plaques (10 × objective). The transmission image indicates any ill-defined opaque obstacle. Only at sub-second repetition rates provided by Milliview can a pathologist diagnose the disordered core and the radial arrangement of refracting elements so as to positively identify the objects 1, 2 and 3 as Alzheimer's disease plaques. (c): Once identified, a further detailed characterization is possible with Milliview at 40× magnification. Further improvements in camera resolution and computer speed may allow in future embodiments of the technology sufficient recognition even at lower magnifications without any time penalty. Images were collected at a wavelength of 550 nm.

approach could open the possibility of measuring some of the tensorial anisotropy of the electro-optic effect in a single sample. Because of the speed of Milliview, integrating several hundreds of difference images obtained for alternating fields within reasonable time could result in high-resolution electro-optic effect measurements. Further research is obviously needed.

Dichroic crystal

A general problem arises if a sample exhibits linear dichroism as that would affect the measurement of $|\sin(\delta)|$. A remedy would be to choose a wavelength outside the region of absorption if that is possible. However, linear dichroism can be measured independently from linear birefringence (where the absorption anisotropy is seen in projection to the fast and slow axes of the birefringent sample).

Crystals grown from solutions containing a dilute dye additive may incorporate the dye molecules into the lattice (Kahr & Gurney, 2001). During this process the molecules become aligned causing linear dichroism. The Milliview set-up, without circular polarizer, was used to image linear dichroism (see, e.g. Kaminsky *et al.*, 2004).

Figure 12 shows an example of a phthalic acid (*ortho*-$C_6H_4(CO_2H)_2$) crystal grown in the presence of the acid-base indicator methyl red. The dye populated only {110} and {001} growth sectors, but in different states, causing a bow-tie–like impression (Benedict *et al.*, 2006).

Discussion

In transforming a sequence of images usually collected in time into an instantaneous process spread in space, all required data are collected in a single image for the analysis of linear anisotropies, thus overcoming sampling rate limitations of other polarized light microscopies. The limiting factor is only the sampling speed of the camera. In the on-line mode, with the false-coloured images of $|\sin(\delta)|$, φ, and

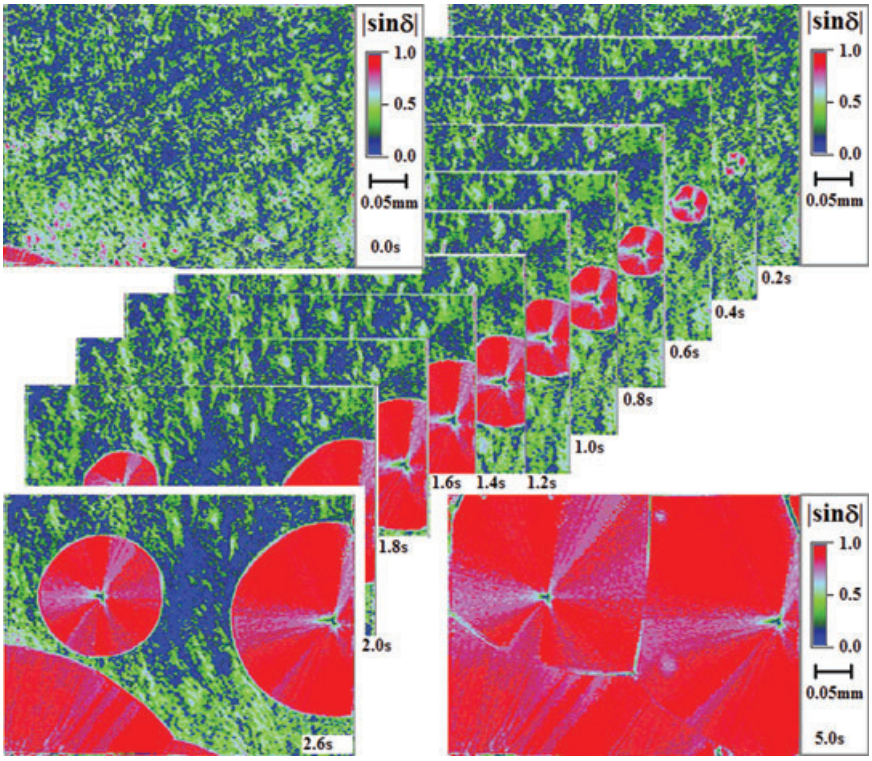

Fig. 10. Growth of spherulites from the 80:20 cholesterylacetate–cholesterylbenzoate liquid crystalline state visible as irregular birefringence pattern in the background.

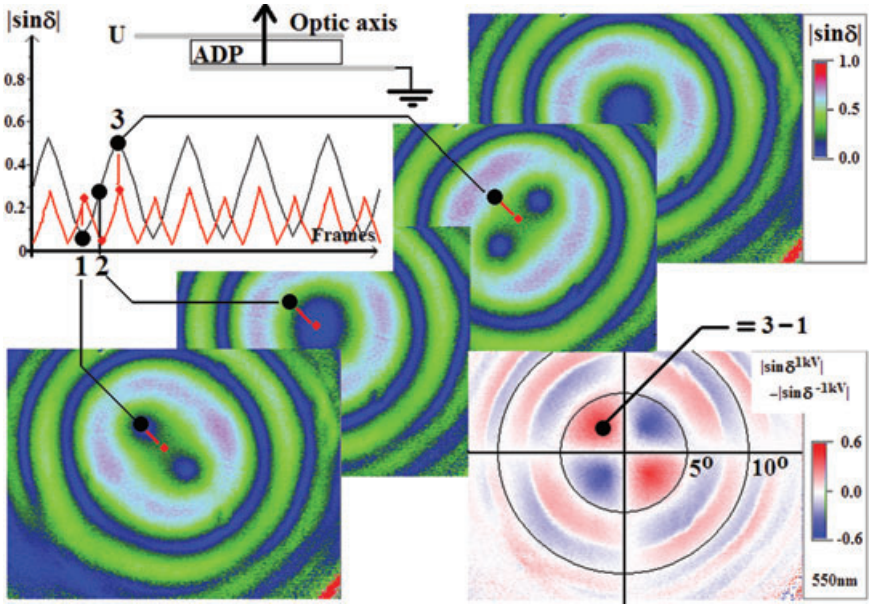

Fig. 11. Conoscopic image of a $(NH_4)H_2PO_4$ crystal cut normal to the *c*-axis (optic axis) of the tetragonal reference system. The crystal becomes biaxial in an applied electric field. The line chart shows the variation of birefringence in a modulated field. The insert on the bottom right shows a difference image between the images at +1 kV and −1 kV along [001].

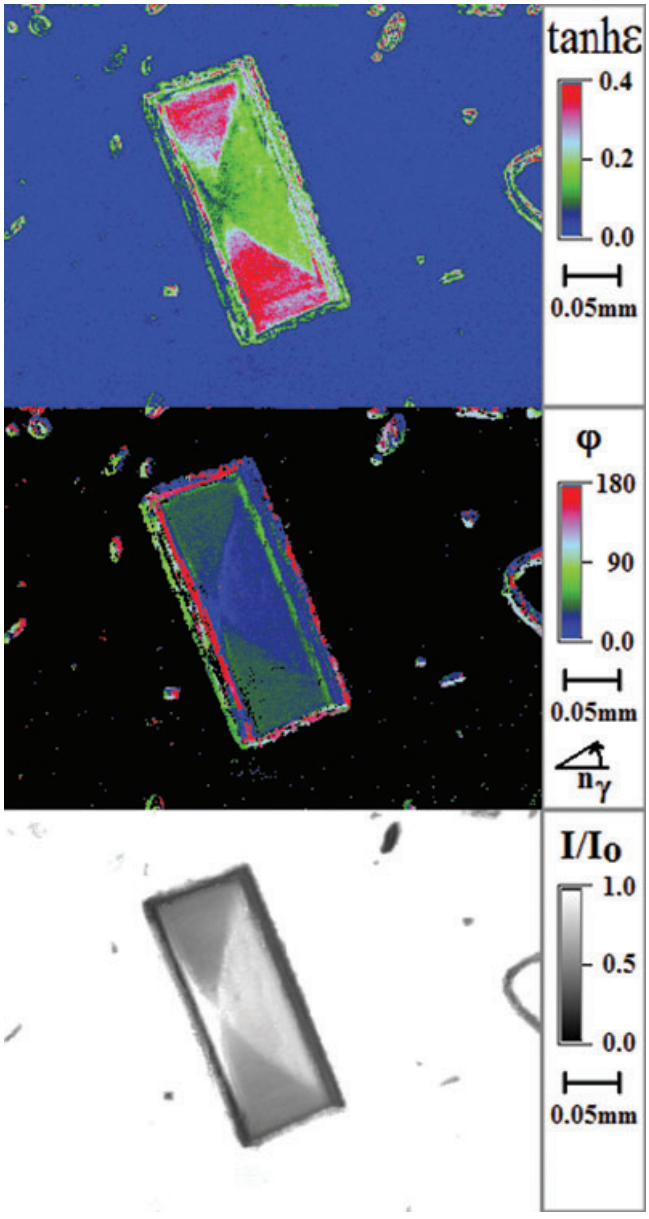

Fig. 12. Linear dichroism in *ortho*-$C_6H_4(CO_2H)_2$) crystal grown in the presence of the acid–base indicator methyl red. The dye populated only {110} and {001} growth sectors, but in different states. The property ε is related to the absorption for light polarized along (a'') and perpendicular (a') to those growth sectors: $\varepsilon = (a'' - a')/2$.

transmittance calculated immediately after collecting the first image, Milliview still reaches repetition rates faster than 10 s^{-1} on state-of-the-art computers with $\geq$2.6 GHz clock frequencies.

Milliview addresses applications where the emphasis lies on speed rather than spatial resolution. Even 1-s sampling times can be stressful when manually screening a sample. Milliview was found to obviate discomfort when screening tissues for birefringent amyloid plaques.

Milliview shows promise for large-scale, automated protein crystal growth. Techniques developed previously, despite being able to detect proteins on the basis of their birefringence (Echalier *et al.*, 2003; Nollert, 2003; Owen & Garman[2], 2005; Kawabata *et al.*, 2006), are either too slow for automatic screening of the large number of samples generated by the novel proteomic techniques or too inaccurate (Asundi *et al.*, 2001).

No method to date will permit the dynamic analysis of birefringence, eigenrays and transmittance images of living organisms. The typical movements of microscopic organisms occur on a timeframe of $\leq$30 Hz. Sampling of a water flea in off-line mode showed that Milliview can make accurate measurements of birefringence and associated features without the need of constraining or disabling the animal.

Where the time derivative of the object reaches large values, different camera methods may be employed to answer the needs of short sampling times. After capturing a movie of the event, the video file can be analyzed off-line to extract the component images. Without moving parts, Milliview is capable of being employed in corrosive environments or those requiring mechanical stability (especially if an optical prism is used to multiplex the images, see later).

Milliview is basically an add-on that can be combined with any polarized light microscope dramatically improving the value and range of the old device. Milliview was shown to work with a >100-year-old Leitz microscope. However, the method is not restricted to microscopic imaging. Any optical imaging system where objects are investigated ellipsometrically would benefit from the approach described here.

In another embodiment of Milliview, a hand ground prism with polarizers affixed gave even better polarimetric results than the commercial image multiplexer (Fig. 13). In this case, a webcam based on CMOS technology with 640 × 480 (real) pixel resolution and 30 frames per second capability was employed. Above, we demonstrated that a camera like those with a CMOS chip which is prone to a drifting gain can still be used for this purpose. In addition, there are negligible parasitic ellipticities introduced, obviating the necessity of producing calibration curves.

The CMOS camera simultaneously produces three images seen through colour filters embedded on the light-sensitive chip. One can take full advantage of this and use the method outlined in Geday *et al.* (2000) to remove the ambiguity of |sin (δ)| and to calculate absolute values for the phase δ from a single image. For this, one needs to illuminate the sample with an RGB-LED in which the colour overlap for red, green and blue is almost completely eliminated. Results of using this approach will be published in a forthcoming report.

[2] The work published by Owen & Garman was inspired and supervised by M.A. Geday.

Fig. 13. A round polarizer seen through a facetted prism with polarizer mask. The total prism's size is 2.5 cm^2. The slopes of the prisms are set to 10° slightly off the body diagonals to represent the correct camera image aspect ratio (1.333). The multiplexed images of the round polarizer are different for each facet depending on the directions of the individual polarizers in the mask for each prism section.

Acknowledgements

The project was funded by a grant to W.K. from Royalty Research Foundation of the University of Washington and a grant to B.K. from the National Science Foundation (USA). A gift, arranged by Luciana Simoncini, was received from the Washington Research Foundation to evaluate possibility of using the prism multiplexer to build a prototype of a commercial device. Thanks to J.B. Benedict for preparing the phthalic acid mixed crystal.

References

Ajovalasit, A., Barone, S. & Petrucci, G. (1998) A review of automated methods for the collection and analysis of photoelastic data. *J. Strain Anal.* **38**, 75–92.

Asundi, A., Tong, L. & Boay, C.G. (2001) Dynamic phase-shifting photoelasticity. *Appl. Opt*. **40**, 3654–3658.

Bajor, A.L. (1995) Automated polarimeter-macroscope for optical mapping of birefringence, azimuths, and transmission in large area wafer. Part I. Theory of the measurement. *Rev. Sci. Instrum*. **66**, 2977–2990.

Benedict, J.B., Cohen, D., Lovell, S., Rohl, A. & Kahr, B. (2006) What is syncrystallization? States of pH indicator methyl red in single phthalic acid crystals. *J. Am. Chem. Soc.* **128**, 5548–5555.

Brandl, Z. (2005) Freshwater copepods and rotifers: predators and their prey. *Hydrobiologia* **546**, 475–489.

de Boer, J.F., Milner, T.E., van Gemert, M.J.C. & Nelson, J.S. (1997) Two-dimensional birefringence imaging in biological tissue by polarization-sensitive optical coherence tomography. *Opt. Lett.* **22**, 934–936.

de Boer, J.F., Milner, T.E. & Nelson, J.S. (1999) Determination of the depth-resolved Stokes parameters of light backscattered from turbid media by use of polarization-sensitive optical coherence tomography. *Opt. Lett.* **24**, 300–302.

Echalier, A., Glazer, R.L., Fülöp, V. & Geday, M.A. (2003) Assessing crystallization droplets using birefringence. *Acta Cryst. Sect. D, Biol. Crystallogr.* **60**, 696–702.

Geday, M.A. & Glazer, A.M. (2004) Birefringence of $SrTiO_3$ at the ferroelastic phase transition. *J. Phys. Cond. Matt.* **16**, 3303–3310.

Geday, A.M., Kaminsky, W., Lewis, J.G. & Glazer, A.M. (2000) Images of absolute retardance L·Δn, using the rotating polarizer method. *J. Microsc.* **198**, 1–9.

Glazer, A.M. & Cosier, J. (1997) Method and apparatus for indicating optical anisotropy. *UK patent application*, 2,310,925 7.

Glazer, A.M., Lewis, J.G. & Kaminsky, W. (1996) A new optical imaging system for birefringent media. *J. Roy. Soc. London* **A452**, 2751–2765.

Hamza, A.A., Fouda, I.M., Sokkar, T.Z.N., Sadik, A.M. & El-Bakary, M.A. (2002) Spectral dispersion curves of polymeric birefringent textile fibers. *J. Appl. Polym. Sci.*, **84**, 2481–2488.

Hartshorne, N.H. & Stuart, A. (1964) *Practical Optical Crystallography*. Edward Arnold, London.

Haussuehl, S. (1983) *Kristallphysik*. Physik-Verlag; Weinheim: Verlag Chemie.

Jin, L-W., Claborn, K., Kurimoto, M., Kaminsy, W., Geday, M., Maezawa, I., Estrada, M. & Kahr, B. (2003) Imaging linear birefringence and dichroism in cerebral amyloid pathologies. *Proc. Natl. Acad. Sci. USA* **100**, 15294–15298.

Kahr, B. & Gurney, R.W. (2001) Dyeing crystals. *Chem. Rev.* **101**, 893–951.

Kaminsky, W., Claborn, K. & Kahr, B. (2004) Polarimetric imaging of crystals. *Chem. Rev. Soc.* **33**, 514–525.

Kawabata, K., Saitoh, K., Takahashi, M., Sugahara, M., Asama, H., Mishima, T. & Miyano, M. (2006) Integrated state evaluation for the images of crystallization droplets utilizing linear and nonlinear classifiers. *Acta Cryst. Sect. D, Biol. Crystallogr.* **62**, 1066–1072.

Landolt-Boernstein (1969) Vol. 3 (New Series): *Ferro and Antiferroelectric Substances*. Springer-Verlag, Berlin.

Litwin, D. & Sadik, A.M. (1998) Measurement of birefringence of textile fibers based on the analysis of the interference pattern in the backfocal plane of the microscope objective. *Proc. SPIE* **3479**, 160–169.

Mei, G. & Oldenbourg, R. (1994) Fast imaging polarimetry with precision universal compensator in polarization analysis and measurement II. (eds. by D.H. Goldstein and D.B. Chenault). *Proc. SPIE* **2265**, 29–39.

Noguchi, M., Ishikawa, T., Ohno, M. & Tachihara, S. (1992) Measurement of 2D birefringence distribution. *International Symposium on Optical Fabrication, Testing, and Surface Evaluation*. (ed. by J. Tsujiuchi.). *Proc. SPIE* **1720**, 367–378.

Nollert, P. (2003) Microscope detection options for colorless protein crystals grown in lipidic cubic phases. *J. Appl. Cryst.* **36**, 1295–1296.

Oldenbourg, R. & Mei, G. (1994) Polarized light microscopy *U.S. patent* 5,521,705 12.

Oldenbourg, R. & Mei, G. (1995) New polarized light microscope with precision universal compensator. *J. Microsc. Oxford* **180**, 140–147.

Otani, Y., Shimada, T., Yoshizawa, T. & Umeda, N. (1994) Two-dimensional birefringence measurement using the phase shifting technique. *Opt. Eng.* **33**, 1604–1609.

Owen, R.L. & Garman, E. (2005) A new method for predetermining the diffraction quality of protein crystals: using SOAP as a selection tool. *Acta Cryst. Sect. D* **61**, 130–140.

Pajdzik, L.A. & Glazer, A.M. (2006) Three-dimensional birefringence imaging with a microscope tilting-stage. I. Uniaxial crystals. *J. Appl. Cryst.* **39**, 326–337.

Saxer, C.E., de Boer, J.F., Park, B.H., Zhao, Y., Chen, Z. & Nelson, J.S. (2000) High-speed fiber-based polarization-sensitive optical coherence tomography of *in vivo* human skin. *Opt. Lett.* **25**, 1355–1357.

Shribak, M.I. (1996) Autocollimating detectors of birefringence. In International Conference on Optical Inspection and Micromeasurements. (ed. by C. Gorecki). *Proc. SPIE* **2782**, 805–813.

Shribak, M.I. & Oldenbourg, R. (2003) Techniques for fast and sensitive measurements of two-dimensional birefringence distributions. *Appl. Opt.* **42**, 3009–3017.

Shribak, M.I., Otani, Y. & Yoshizawa, T. (1999) Return-path polarimeter for two-dimensional birefringence distribution measurement. *Polarization: Measurement, Analysis, and Remote Sensing II*. (eds. by D.H. Goldstein and D.B. Chenault). *Proc. SPIE* **3754**, 144–149.

Velez, H.A. (2003) Identification characteristics of PLA fibers: a new generic fiber type. *Forensic Sci. Commun.* **5**, (http://www.fbi.gov/hq/lab/fsc/backissu/july2003/velez.htm)

Yeh, W.H., Carrier, J. & Mansuripur, M. (1999) Polarization microscopy of magnetic domains for magneto-optical disks. *Appl. Opt.* **38**, 3749–3758.

Zeitner, U.D., Kaufmann, S., Kley, E.-B. & Herzig, H.P. (2003) Micro-optical sensor system for birefringence characterization of textile-fibers. *Proc. SPIE* **5183**, 79–84.

Zernicke, F. (1964) Refractive indices of ADP and KDP between 2000Å and 1.5 μm. *J. Opt. Soc. Am.* **54**, 1215–1220.

Zhu, Y., Koyama, T., Takada, T. & Murooka, Y. (1999) Two-dimensional measurement technique for birefringence vector distributions: measurement principle. *Appl. Opt.* **38**, 2225–2231.

Zhu, Y., Takada, T. & Murooka, Y. (2002) Two-dimensional optical measurement techniques based on optical birefringence effects. *Opt. Eng.* **41**, 3183–3192.

